Pure Appl. Geophys. 179 (2022), 4521–4539

https://doi.org/10.1007/s00024-022-03156-z

Pure and Applied Geophysics

Rheological Model for a Vertically Fractured Source Rock

GUANGTAN HUANG,[1] JING BA,[2] JOSÉ M. CARCIONE,[3] and WEIHUA LIU[4]

Abstract—The elastic stress–strain relation of deep source rocks must account for the presence of fractures and lamination due to thermally mature kerogen layers. Clay lamination describes the variation in transverse isotropy with a vertical symmetry (VTI) characteristic of shale background, and vertical fractures induce the transverse isotropy with a horizontal symmetry (HTI) perturbations. Thus, the fractured shale rock can be described as a medium with an orthorhombic symmetry in terms of effective anisotropy. We present a new workflow for calculating the elastic constants of a pressure-dependent fractured shale rock and the effects of clay lamination and microfractures. We investigate the shale fabric that can result in the orthorhombic elastic symmetry and the effect of pressure on elastic parameters, and propose an inversion methodology. Results based on well-log data show that the proposed methodology can be effectively applied to field data.

Keywords: Shale source rock, elasticity, pressure, microfractures, anisotropy.

1. *Introduction*

Deep shale-gas resources are subject to high in situ confining stress and possess complex microfracture patterns and clay and kerogen lamination, leading to effective low-symmetry seismic anisotropy in the orthotropic (orthorhombic) and monoclinic classes (Carcione et al., 2012a, b; Li et al., 2015). Carcione (2000) developed a model to describe the anelastic properties of shales with transverse isotropy and calculated the excess pore pressure as a function of the fraction of kerogen converted to oil (shale maturation). Rock-physics templates for clay-rich source rocks were proposed by Carcione and Avseth (2015) to detect the degree of maturation from seismic properties. Due to its ductile behavior, shale is more likely to be compacted than other sedimentary rocks (Wang, 2002). Compaction and diagenesis have a significant impact on rock elasticity, as well as on shale brittleness (Carcione et al., 2021). Scanning electron microscopy (SEM) images reveal that shale has a clay lamination with varying preferred orientation angles (Hornby et al., 1994), leading to low-symmetry anisotropy. Johnston and Christensen (1995) experimentally found that a strong positive correlation exists between the preferred orientation of clays (illite), as expressed in the orientation indices, and seismic anisotropy. Sayers (2005) and Xu et al. (2010) proposed an orientation distribution function (ODF) to represent the mineral and pore alignments. Qian et al. (2016) assumed that the ODF is a normal distribution with a zero mean, and used a lamination index (LI) to parameterize the variable standard deviation. Zhang et al. (2017) and Zhang (2017) developed a rock-physics model to describe the rheology of the shale with preferred clay particle orientations, based on the Bond transform (Bond, 1943) and Voigt–Reuss–Hill (VRH) average (Hill, 1952; Mavko et al., 2020).

Vertically fractured shale reservoirs can be considered orthotropic, unlike shales without microfractures, which exhibit transverse isotropy media with a vertical axis of symmetry (VTI). Fractures are commonly developed in deep shale reservoirs under the effect of in situ stress (Crampin, 1984; Hsu and Schoenberg, 1993; Carcione et al., 2012a; Carcione and Picotti, 2012; Bakulin et al., 2000a, b; Carcione et al., 2013; Oh and Alkhalifah, 2016). Microfracture information can be used to estimate the in situ stress distribution and rock

---

[1] State Key Laboratory of Geomechanics and Geotechnical Engineering, Institute of Rock and Soil Mechanics, Chinese Academy of Sciences, Wuhan 430071, Hubei, China.

[2] School of Earth Sciences and Engineering, Hohai University, Nanjing 211100, China. E-mail: jba@hhu.edu.cn

[3] National Institute of Oceanography and Applied Geophysics-OGS, Trieste, Italy.

[4] SINOPEC Geophysical Research Institute, Beijing, China.

brittleness. Early models for fractured rocks have been developed by Hudson (1981) and Schoenberg (1980), assuming an isotropic background medium.

In situ stress and confining pressure have a major effect on microfracture porosity and stiffness. Zimmerman (1991) estimated the compressibility of sandstones and determined their pore aspect ratio distribution using an empirical relation between velocity and pressure. Daley et al. (2006) proposed a method for estimating the normal and tangential fracture compliance Z_N and Z_T as a function of pressure, and David and Zimmerman (2012) extended the method to predict velocities as a function of differential pressure, hereafter called the DZ model (Zhang et al., 2019). Very high compliance occurs at low normal effective stress, approaching low values asymptotically as this stress increases.

Many factors, such as the effect of the clay lamination, the spatial distribution of microfractures, and the in situ effective pressure, must be considered, as well as the maturation process (e.g., Pinna et al., 2011). We consider a model of shale with orthotropic anisotropy. First, we review some related equivalent models and then propose a workflow for a pressure-dependent model. Then, we analyze the influence of the LI, fracture density, and pressure on the rock elasticities. Moreover, we develop an inversion strategy for retrieving these properties from well-log data and present some examples.

2. Methodology

2.1. Effective-medium Theories

Generally, rocks with inclusions are effectively anisotropically homogeneous at a certain scale compared to the wavelength, with the properties equivalent to a heterogeneous solid with embedded inclusions. Typical effective-medium theories are that of Kuster and Toksöz, the Mori-Tanaka method, the self-consistent approximation (SCA), and the differential effective medium (DEM) (see Mavko et al., 2020). Here, we consider the SCA and DEM approaches.

2.1.1 SCA Theory

In the isotropic case, the self-consistent approximation for an N-phase mixture has as solutions the bulk and shear moduli K_{sca} and μ_{sca} obtained from

$$\begin{aligned} &\sum_{j=1}^{N} v_j\left(K_j - K_{\text{sca}}\right)P_j = 0, \\ &\sum_{j=1}^{N} v_j\left(\mu_j - \mu_{\text{sca}}\right)Q_j = 0. \end{aligned} \tag{1}$$

(Willis, 1977; Berryman, 1980), where K_j and μ_j are the bulk and shear modulus, respectively, of the jth phase, P and Q are related to the shape of each inclusion, and v denotes the volume fraction of each phase (e.g., Carcione et al., 2020).

In the anisotropic case, the bulk and shear moduli are replaced by the matrix $\mathbf{C}_{\text{sca}}$, such that

$$\begin{aligned} \mathbf{C}_{\text{sca}} = &\sum_{i=1}^{M} v_i\mathbf{C}_i\left(\mathbf{I} + \hat{\mathbf{G}}(\mathbf{C}_i - \mathbf{C}_{\text{sca}})\right)^{-1} \\ &\left\{\sum_{j=1}^{N} v_j\left[\mathbf{I} + \hat{\mathbf{G}}\left(\mathbf{C}_j - \mathbf{C}_{\text{sca}}\right)\right]^{-1}\right\}^{-1} \end{aligned} \tag{2}$$

(Hornby et al., 1994), where

$$\hat{\mathbf{G}}_{ijkl} = \frac{1}{8\pi}\left(\overline{\mathbf{G}}_{ikjl} + \overline{\mathbf{G}}_{jkil}\right) \tag{3}$$

is the Eshelby tensor, $\mathbf{I}$ is the identity matrix, the tensor $\overline{\mathbf{G}}$ can be calculated numerically for the special anisotropic case (Lin and Mura, 1973; Mura, 1991), and $\mathbf{C}_i$ denotes the stiffness matrix related to the ith phase. The inclusions are stated as being connected throughout a limited range of the volume fraction, which is a disadvantage of the SCA method.

2.1.2 DEM Theory

In this case, the inclusions are sequentially added and embedded into the host material, where different orders of inclusion yield different results. The solution $\mathbf{C}_{\text{dem}}$ is obtained from

$$\frac{d}{dv}\left[\mathbf{C}_{\mathrm{dem}}(v)\right] = \frac{1}{(1-v)}\left[\mathbf{C}_i - \mathbf{C}_{\mathrm{dem}}(v)\right] K_i(v)\mathbf{C}_{\mathrm{dem}}(v) \quad (4)$$

(Hornby et al., 1994; Mukerji et al., 1995), where v_i denotes the volume fraction of ith phase, and

$$K_i(v) = \left[\mathbf{C}_{\mathrm{dem}}\left(\mathbf{I} + \hat{\mathbf{G}}\left(\mathbf{C}_i - \mathbf{C}_{\mathrm{dem}}(v)\right)\right)\right]^{-1}. \quad (5)$$

The DEM approach does, however, have a significant disadvantage in that one must first set a host matrix before adding the other inclusions one at a time. Predictions can vary depending on the sequence.

2.1.3 Combined SCA-DEM Method

To overcome the disadvantages of the SCA and DEM methods, Hornby et al. (1994) combined the two approaches (SCA-DEM). Firstly, the SCA is implemented to obtain an effective medium with equal concentration (50% each for two components). Then, this medium is adjusted to the desired concentration by using the DEM method. The advantage of the DEM method is that it can preserve the connectivity of any given phase. The SCA-DEM method does not require setting the host phase, thus avoiding the disadvantage of the DEM method (Guo et al., 2013, 2014).

2.2. Effect of Kerogen Maturity

Electron microscope analysis (Zhao et al., 2016) reveals that the kerogen distribution depends on the maturation stage.

(1) In the immature case, kerogen is distributed in layers and plays a load-bearing role (Vernik and Landis, 1996; Vernik and Liu, 1997; Ahmadov, 2011). The shale elasticities can be obtained with the Backus average (Backus, 1962).

(2) In the mature case, kerogen is converted to oil in the form of bubble inclusions (e.g., Carcione, 2000; Pinna et al., 2011). Kerogen particles are connected with the matrix and hence still play a load-bearing role. Meanwhile, the kerogen-related pores are generated due to the thermal conversion of kerogen to oil (Tissot et al., 1974; Derbyshire, 1991). The DEM method can be used to obtain the stiffness of porous kerogen and add it to the host iteratively.

(3) In the over-mature case, the volume of pore fluid increases, and oil is converted to gas. Instead of the load-bearing matrix, organic material is regarded as an inclusion space filler. The solid substitution equation (Ciz and Shapiro, 2007) is utilized to capture the combined effect of the organic matter–fluid mixture on the overall elastic characteristics of organic shale since the shear modulus of the organic matter–fluid mixture is not zero (Luo and Vasseur, 1996; Vernik and Landis, 1996; Yenugu and Han, 2013). In this case, the load-bearing phase is the clay mineral. The stiffness values are obtained by solid substitution (e.g., Carcione et al., 2011), where the moduli of the dry rock (frame) are obtained with the DEM method.

2.3. Effects of Pores and Kerogen

Generally, pores in shale are mainly divided into two types. The total porosity ϕ of the shale is

$$\phi = \phi_c + \phi_s, \quad (6)$$

(Xu and White, 1995), where ϕ_c and ϕ_s refer to the porosities of “clay-related” voids and “silt-related” voids. The isotropic SCA-DEM can be adopted to include the “silt-related” pores, and the anisotropic SCA-DEM method can be exploited to ensure the connectivity of the “clay-related” pores. Clay-related pores are saturated with fluids and partially aligned, and such preferred orientation affects the elastic anisotropy, as well as the kerogen layers, making the medium VTI.

Kerogen has low bulk and shear moduli (2.9 and 2.7 GPa) (Mavko et al., 2020) compared with those of quartz (37 and 44 GPa) (Mavko et al., 2020) and can be treated as pore infill, as in Carcione et al. (2011). Here, we use the anisotropic SCA-DEM method to include the clay-related pores and kerogen to the clay and then obtain the properties of the solid clay-kerogen mixture.

2.4. *Effect of the Preferred Orientation of the Clay-Kerogen Mixture*

The clay-kerogen mixture has a preferred orientation and contributes greatly to the anisotropy of the shale (Jones and Wang, 1981; Vernik and Nur, 1992; Bandyopadhyay, 2009; Bandyopadhyay et al., 2012). The ODF is assumed to be a normal distribution function as

$$\mathrm{ODF} \sim N(\mathrm{mean}, \mathrm{LI}), \tag{7}$$

where mean denotes the mean value of the angle of tilt, which generally is zero since most of the mixtures remain flat. Thus, the probability density function or volume fraction of preferred orientation is

$$v(\theta, \mathrm{LI}) = \frac{1}{\sqrt{2\pi}} \exp\left(-\frac{\theta^2}{2\mathrm{LI}^2}\right), \tag{8}$$

where θ is the tilt angle. The effective elastic stiffness and compliance of the mixture are estimated by using the VRH average,

$$\begin{aligned} \mathbf{C}_{\mathrm{mix}} &= \frac{1}{2\pi}\int_0^{2\pi}\int_{-\pi/2}^{\pi/2} v(\theta, \mathrm{LI})\mathbf{C}_{\mathrm{rot}}(\theta,\varphi)d\theta d\varphi \\ \mathbf{S}_{\mathrm{mix}} &= \frac{1}{2\pi}\int_0^{2\pi}\int_{-\pi/2}^{\pi/2} v(\theta, \mathrm{LI})\mathbf{S}_{\mathrm{rot}}(\theta,\varphi)d\theta d\varphi \ , \\ \mathbf{C}_{\mathrm{clay}} &= \frac{\mathbf{C}_{\mathrm{mix}} + (\mathbf{S}_{\mathrm{mix}})^{-1}}{2}. \end{aligned} \tag{9}$$

(Hornby et al., 1994), where φ is the azimuth angle, $\mathbf{C}_{\mathrm{rot}}(\theta,\varphi)$ and $\mathbf{S}_{\mathrm{rot}}(\theta,\varphi)$ denote the stiffness and compliance matrices, respectively, of the rotated clay-kerogen mixtures by the Bond transformation

$$\begin{aligned} \mathbf{C}_{\mathrm{rot}}(\theta,0) &= \mathbf{L}_{im}\mathbf{L}_{jn}\mathbf{L}_{kp}\mathbf{L}_{lp}\mathbf{C}_{\mathrm{ck}}(0,0) \\ \mathbf{C}_{\mathrm{rot}}(\theta,\varphi) &= \mathbf{L}_{im}\mathbf{L}_{jn}\mathbf{L}_{kp}\mathbf{L}_{lp}\mathbf{C}_{\mathrm{ck}}(\theta,0) \end{aligned} \tag{10}$$

(Bond, 1943), where $\mathbf{C}_{\mathrm{CK}}$ is the stiffness of the mixture of clay and Kerogen by using DEM theory, and

$$\begin{aligned} \mathbf{L}_\theta &= \begin{bmatrix} 1 & 0 & 0 \\ 0 & \cos\theta & -\sin\theta \\ 0 & \sin\theta & \cos\theta \end{bmatrix}, \\ \mathbf{L}_\varphi &= \begin{bmatrix} \cos\varphi & -\sin\varphi & 0 \\ \sin\varphi & \cos\varphi & 0 \\ 0 & 0 & 1 \end{bmatrix}. \end{aligned} \tag{11}$$

2.5. *Effect of Fractures*

We employ the Schoenberg linear slip model to include the microfractures. According to the linear slip model, the effective compliance of the fractured rock is

$$\mathbf{S}_{\mathrm{frac}} = \mathbf{S}_{\mathrm{b}} + \sum_{i=1}^{L} \alpha_i \mathbf{S}_{f,i}, \tag{12}$$

(Schoenberg, 1980), where $\mathbf{S}_b$ corresponds to the non-fractured shale, $\mathbf{S}_{f,i}$ is the compliance of the ith set of microfractures, and α_i denotes the fraction of the microfracture set. We assume that a group of microfractures perpendicular to the x_1-axis (vertical direction) without cross-coupling develop in the host rock. $\mathbf{S}_f$ can be simplified as

$$\mathbf{S}_f = \begin{bmatrix} Z_N & 0 & 0 & 0 & 0 & 0 \\ 0 & 0 & 0 & 0 & 0 & 0 \\ 0 & 0 & 0 & 0 & 0 & 0 \\ 0 & 0 & 0 & 0 & 0 & 0 \\ 0 & 0 & 0 & 0 & Z_V & 0 \\ 0 & 0 & 0 & 0 & 0 & Z_H \end{bmatrix} \tag{13}$$

(Schoenberg and Sayers, 1995), where Z_N is the normal compliance, Z_V is the vertical tangential compliance, and Z_H is the horizontal tangential compliance of the fractures. For one set of vertical microfractures, the shale is an orthotropic medium. The stiffness matrix is given by

$$\mathbf{C}_{\mathrm{ORT}}=\begin{bmatrix} c_{11} & c_{12} & c_{13} & 0 & 0 & 0\\ c_{21} & c_{22} & c_{23} & 0 & 0 & 0\\ c_{31} & c_{32} & c_{33} & 0 & 0 & 0\\ 0 & 0 & 0 & c_{44} & 0 & 0\\ 0 & 0 & 0 & 0 & c_{55} & 0\\ 0 & 0 & 0 & 0 & 0 & c_{66}\end{bmatrix}$$

$$=\begin{bmatrix} c_{b,11}(1-\delta_N) & c_{b,12}(1-\delta_N) & c_{b,13}(1-\delta_N) & 0 & 0 & 0\\ c_{b,12}(1-\delta_N) & c_{b,11}\left(1-\delta_N\dfrac{c_{b,12}^2}{c_{b,11}^2}\right) & c_{b,13}\left(1-\delta_N\dfrac{c_{b,12}}{c_{b,11}}\right) & 0 & 0 & 0\\ c_{b,13}(1-\delta_N) & c_{b,13}\left(1-\delta_N\dfrac{c_{b,12}}{c_{b,11}}\right) & c_{b,33}\left(1-\delta_N\dfrac{c_{b,13}^2}{c_{b,11}c_{b,33}}\right) & 0 & 0 & 0\\ 0 & 0 & 0 & c_{b,44} & 0 & 0\\ 0 & 0 & 0 & & c_{b,44}(1-\delta_V) & 0\\ 0 & 0 & 0 & 0 & 0 & c_{b,66}(1-\delta_H)\end{bmatrix} \tag{14}$$

(Schoenberg and Douma, 1988). Thus,

$$\Delta\mathbf{C}=\begin{bmatrix} -c_{b,11}\delta_N & -c_{b,12}\delta_N & -c_{b,13}\delta_N & 0 & 0 & 0\\ -c_{b,12}\delta_N & -\dfrac{c_{b,12}^2}{c_{b,11}}\delta_N & -\dfrac{c_{b,12}c_{b,13}}{c_{b,11}}\delta_N & 0 & 0 & 0\\ -c_{b,13}\delta_N & -\dfrac{c_{b,12}c_{b,13}}{c_{b,11}}\delta_N & -\dfrac{c_{b,13}^2}{c_{b,11}}\delta_N & 0 & 0 & 0\\ 0 & 0 & 0 & 0 & 0 & 0\\ 0 & 0 & 0 & & -c_{b,44}\delta_V & 0\\ 0 & 0 & 0 & 0 & 0 & -c_{b,66}\delta_H\end{bmatrix}. \tag{15}$$

Hsu and Schoenberg (1993) introduced the fracture weaknesses to quantitatively represent Z_N, Z_V, and Z_H

$$\delta_N=\frac{c_{b,11}Z_N}{1+c_{b,11}Z_N},\quad \delta_V=\frac{c_{b,44}Z_V}{1+c_{b,44}Z_V},\quad \delta_H=\frac{c_{b,66}Z_H}{1+c_{b,66}Z_H}. \tag{16}$$

According to Hudson (1981), when the direction of fracture set is perpendicular to the x_1-axis, the first-order correction is

$$C_{ipjq}^1=-\frac{e}{\mu}C_{b,k1ip}C_{b,l1jq}U_{kl}, \tag{17}$$

where e denotes the fracture density, and U_{kl} are the fracture-related parameters. The symmetry of the problem shows that U_{kl} is diagonal and that $U_{22} = U_{33}$ (Hudson, 1981). Moreover, using the Voigt notation, the first and second pairs of suffixes of the fourth-order tensors can be rewritten as

$$\begin{aligned} &(1,1) \to 1, \quad (2,2) \to 2, \quad (3,3) \to 3, \\ &(2,3) \to 4, \quad (1,3) \to 5, \quad (1,2) \to 6. \end{aligned} \tag{18}$$

Then,

$$\mathbf{C}^1 = -\frac{e}{\mu}\begin{bmatrix} c_{b,11}^2 U_{11} & c_{b,11}c_{b,12}U_{11} & c_{b,11}c_{b,13}U_{11} & 0 & 0 & 0 \\ c_{b,11}c_{b,12}U_{11} & c_{b,12}c_{b,12}U_{11} & c_{b,13}c_{b,12}U_{11} & 0 & 0 & 0 \\ c_{b,11}c_{b,13}U_{11} & c_{b,13}c_{b,12}U_{11} & c_{b,13}^2 U_{11} & 0 & 0 & 0 \\ 0 & 0 & 0 & 0 & 0 & 0 \\ 0 & 0 & 0 & 0 & c_{b,55}^2 U_{33} & 0 \\ 0 & 0 & 0 & 0 & 0 & c_{b,66}^2 U_{33} \end{bmatrix}. \tag{19}$$

We express U_{11} and U_{33} as

$$\begin{aligned} U_{11} &= \frac{4(\lambda + 2\mu)}{3(\lambda + \mu)}\frac{1}{1+k}, \\ U_{33} &= \frac{16(\lambda + 2\mu)}{3(3\lambda + 4\mu)}\frac{1}{1+M}, \end{aligned} \tag{20}$$

where k and M are microfracture related parameters

$$\begin{aligned} k &= \frac{\lambda + 2\mu}{\pi\chi\mu(\lambda + 2\mu)}\left(K' + \frac{4}{3}\mu'\right), \\ M &= \frac{4\mu'(\lambda + 2\mu)}{\pi\chi\mu(\lambda + \mu)}, \end{aligned} \tag{21}$$

and K' and μ' denote the bulk and shear moduli of the fracture infill, respectively. Compared with Eqs. (15) and (19), we obtain

$$\delta_N = \frac{c_{b,11}}{c_{b,44}}eU_{11}, \quad \delta_V = \frac{c_{b,55}}{c_{b,44}}eU_{33}, \quad \delta_H = \frac{c_{b,66}}{c_{b,44}}eU_{33}. \tag{22}$$

2.6. *Pressure-Dependent Fracture Model*

According to the DZ model (Daley et al., 2006), the fracture compliance values are

$$\begin{aligned} Z_V &= Z_{V\infty} + [Z_{V0} - Z_{V\infty}]\exp(-\sigma_{11}/\tau_V), \\ Z_H &= Z_{V\infty} + [Z_{H0} - Z_{V\infty}]\exp(-\sigma_{11}/\tau_H), \\ Z_N &= Z_{N\infty} + [Z_{N0} - Z_{N\infty}]\exp(-\sigma_{11}/\tau_N), \end{aligned} \tag{23}$$

and the compliance matrix of the host rock is

$$\mathbf{S}_b = \mathbf{S}_{b\infty} + [\mathbf{S}_{b0} - \mathbf{S}_{b\infty}]\exp(-\sigma_{11}/\tau_S) \tag{24}$$

(David and Zimmerman, 2012), where τ_S, τ_N, τ_V, and τ_H are the decay constants for $\mathbf{S}_b$, Z_N, Z_V , and Z_H, respectively, $\mathbf{S}_{b0}$, Z_{N0}, Z_{V0} , and Z_{H0} denote the matrix and microfracture compliance under zero pressure, and $\mathbf{S}_{b\infty}$, $Z_{N\infty}$, $Z_{V\infty}$, and $Z_{H\infty}$ correspond to the compliance at very high pressure. Here, the pressure refers to σ_{11}, i.e., vertical stress.

Thus, the workflow of the proposed rock-physics model as given in Fig. 1 is as follows:

(1) The clay minerals, i.e., illite, montmorillonite, kaolinite, and chlorite, are mixed using the Backus average according to their volume fractions, and the anisotropic SCA-DEM algorithm is used to add kerogen and clay-related pores into the mixed clay minerals to obtain the clay-kerogen mixture. In this work, we consider a homogeneous mixture of fine-grained clay minerals. Published data exist for the stiffness tensor of anisotropic clay even with allowance made for formation water effect (e.g., Sayers and den Boer, 2018; Bayuk et al., 2007). If the clay anisotropy is taken into account, an additional modeling procedure with the anisotropic SCA-DEM can be adopted in a future study.

(2) Based on LI obtained from well-log data, the Bond transformation is used to rotate the clay-kerogen mixture according to the normal

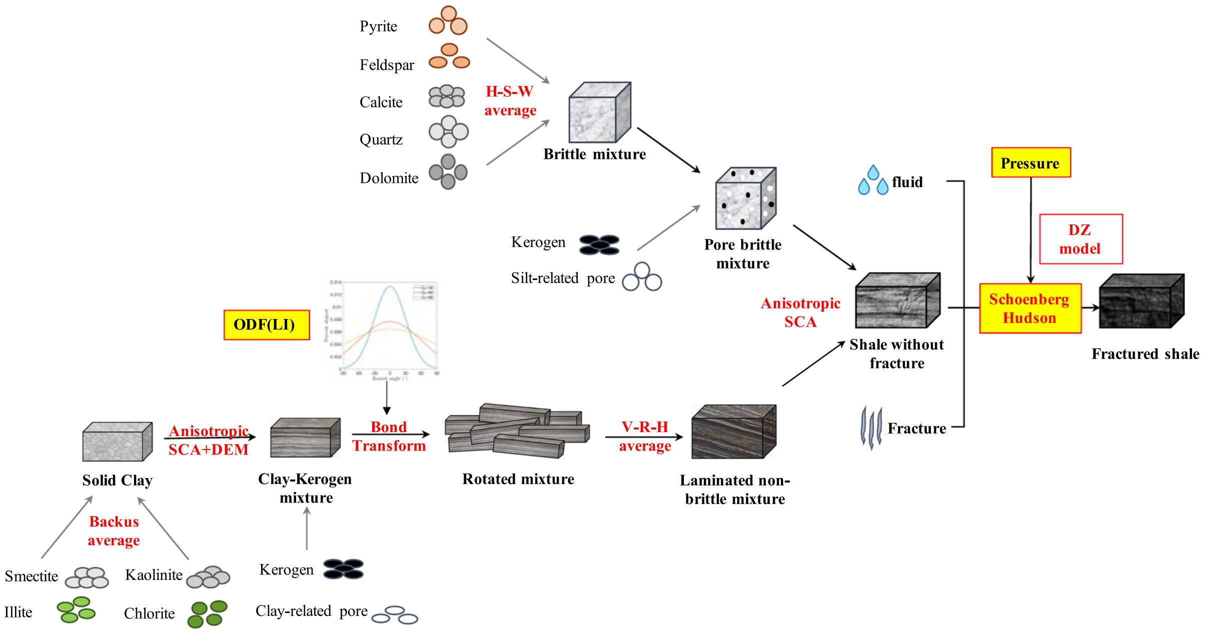

Figure 1

Workflow of the proposed model. The elasticities of shale background (the left-hand side section) is constructed with clay lamination, followed by the introduction of fractures with the Schoenberg model and using the DZ model for a pressure-dependent fractured shale rock

distribution, and the VRH average is used to obtain the stiffness values of the preferred orientated clay-kerogen mixture.

(3) The VRH average is used to mix the brittle minerals, such as quartz, feldspar, pyrite, dolomite, and calcite, according to their volume fractions, and the SCA-DEM algorithm is applied to add kerogen and stiff pores into the brittle minerals to derive the stiffness values of the mixed brittle mixture.

Table 1

Elastic properties of the minerals

Minerals		V_P (km/s)	V_S (km/s)	ρ (g/cm^3)	Source
Clay	Illite	4.15	1.9	2.55	Eastwood and Castagna (1987)
	Smecitite	2.3	1.3	2.29	Vanorio et al. (2003)
	Kaolinite	2.71	1.52	2.59	Vanorio et al. (2003)
	Chlorite	3.713	1.634	2.69	Hui et al. (2011); Wang et al. (2001)
Brittle	Quartz	6.008	4.075	2.65	Carmichael (1988)
	Feldspar	4.680	2.39	2.62	Mavko et al. (2020)
	Calcite	6.64	3.44	2.71	Simmons (1965)
	Dolomite	7.34	3.96	2.87	Humbert et al. (1972)
	Pyrite	8.011	5.18	4.93	Simmons and Birch (1963)
Fluid		1.47	0	1.04	Guo et al. (2014)

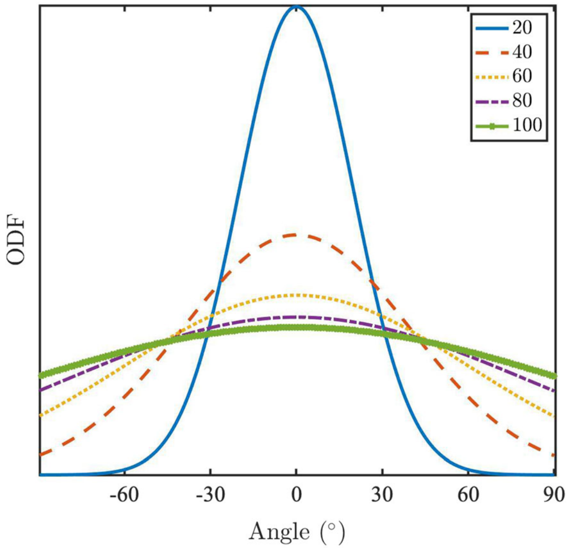

Figure 2

Orientation distribution function for various lamination indices (LI)

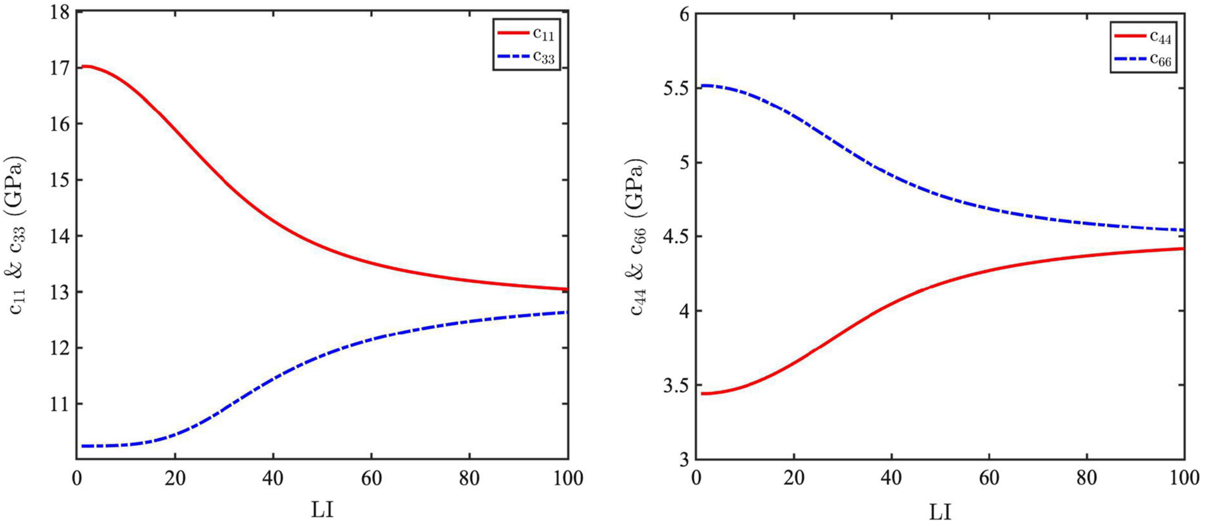

(a) **(b)**

Figure 3
Elasticity: **a** c_{11} and c_{33} and **b** c_{44} and c_{66} as a function of the clay lamination index (LI)

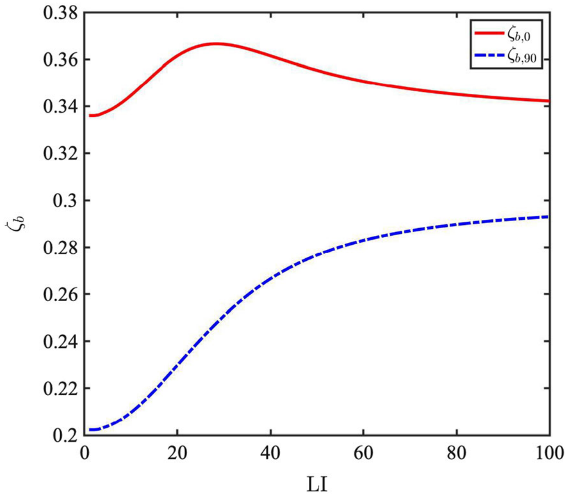

Figure 4
$\zeta_{b,0} = \dfrac{\rho V_{S0}^2}{\rho V_{P0}^2}$ and $\zeta_{b,90} = \dfrac{\rho V_{S90}^2}{\rho V_{P90}^2}$ as a function of LI

(4) The anisotropic SCA method is used to combine the clay-kerogen and brittle mixtures to obtain a shale model without microfractures.
(5) Based on the Schoenberg linear-slip model for fractures, vertical microfractures are added to obtain the stiffness values for the fractured shale.

Table 2
Saturating fluid bulk modulus

Fluid	V_P (km/s)	Density (g/cm^3)
Brine	1.47	1.04
Oil	0.75	0.7
Gas	0.603	0.0011

(6) Based on the DZ model, the relation between the microfracture compliance and pressure is derived, and then we obtain the stiffness values of the fractured shale at the in situ pressure.

3. *Examples*

We consider shales from the formations of the Longmaxi area in southwest China, which have high organic maturity (over-mature), developed microfractures (compressive fractures can be observed in syncline structures), and are subject to high confining pressures. Three aforementioned

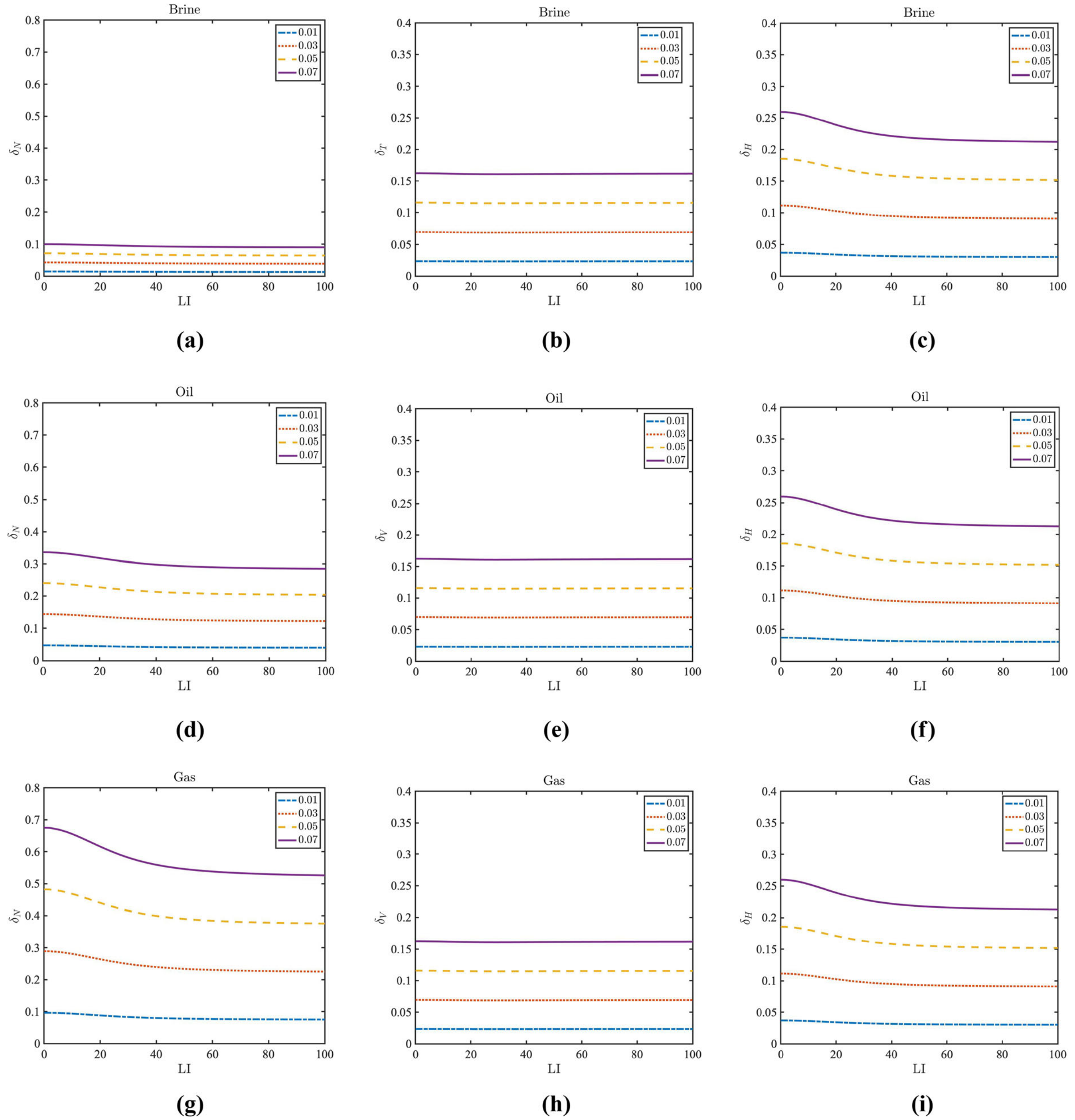

(a) **(b)** **(c)**

(d) **(e)** **(f)**

(g) **(h)** **(i)**

Figure 5

Fracture weaknesses: (**a**, **d**, **g**) δ_N, (**b**, **e**, **h**) δ_V , and (**c**, **f**, **i**) δ_H as a function of LI for various fracture densities *e* and fracture fluid infill

factors are considered in the analysis: LI, microfractures, and confining pressure. According to the workflow of Fig. 1, three models are proposed: (1) a shale model with varying LI but without fracture under a confining pressure; (2) a micro-fractured shale with given LI under normal pressure; and (3) a fractured shale with a give LI under variable pressure. Table 1 shows the elastic parameters of the related minerals.

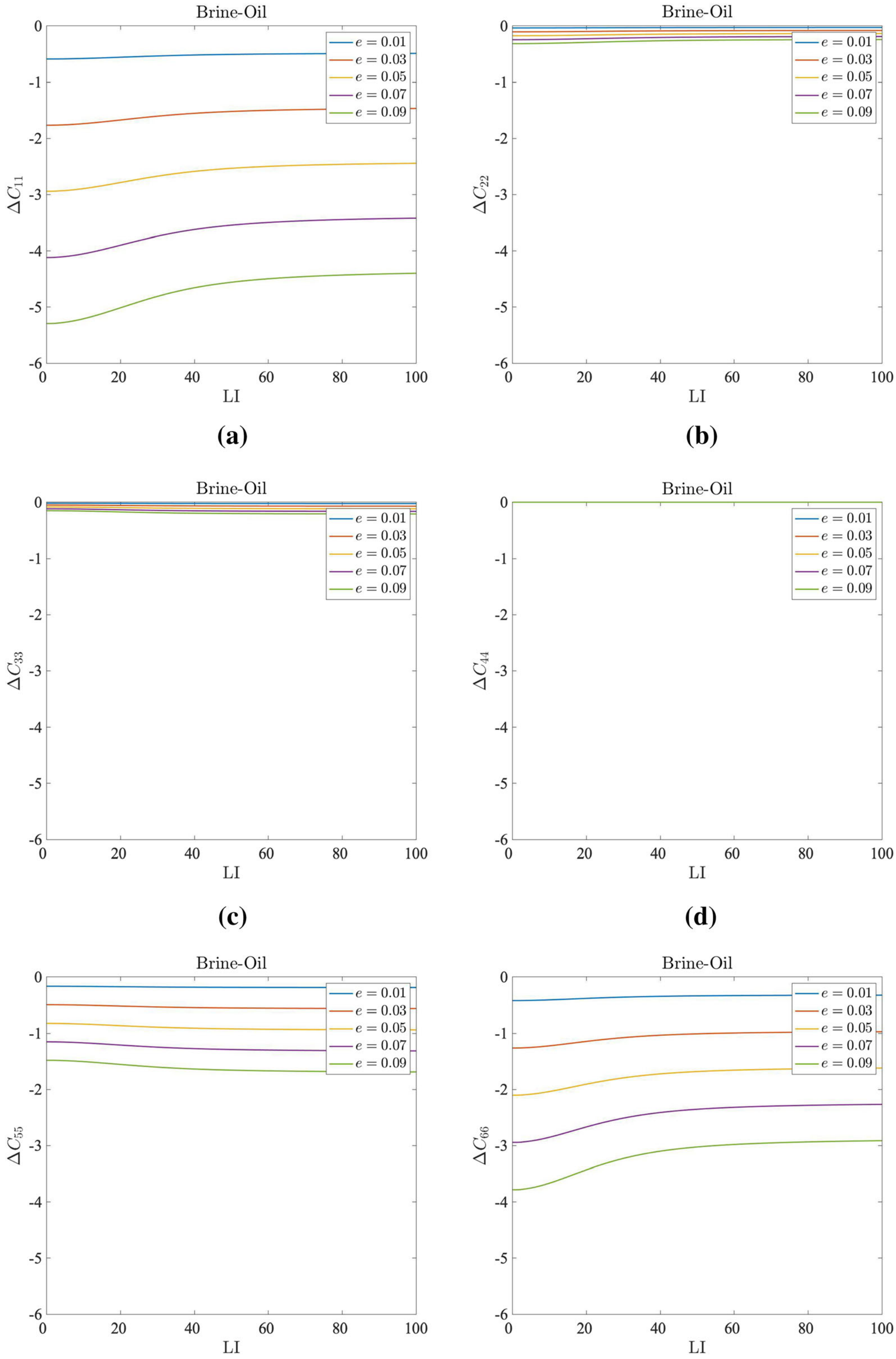
Brine-Oil
ΔC_{11}
ΔC_{22}
ΔC_{33}
ΔC_{44}
ΔC_{55}
ΔC_{66}
LI
0
20
40
60
80
100
0
-1
-2
-3
-4
-5
-6
$e = 0.01$
$e = 0.03$
$e = 0.05$
$e = 0.07$
$e = 0.09$

(a) **(b)**

(c) **(d)**

(e) **(f)**

◀Figure 6
Stiffness coefficient perturbation between the fractured and background shale models: (**a**) Δc_{11}, (**b**) Δc_{22}, (**c**) Δc_{33}, (**d**) Δc_{44}, (**e**) Δc_{55}, and (**f**) Δc_{66} as a function of LI and various fracture densities e and fluid mixtures

3.1. *Effect of the Clay Lamination Index*

The ODF of clay minerals is assumed to be a normal distribution. Since most clay-kerogen mixtures are flat, the mean value of the ODF is set to zero. ODFs with LIs of 20, 40, 60, 80, and 100 are shown in Fig. 2. In the case of low LI, the data are distributed in a narrow range near the mean value. The VTI feature is rapidly weakened as LI increases, implying that some clay-kerogen mixtures are rotated. Figure 3 shows the stiffness c_{11}, c_{33}, c_{44}, and c_{66} as a function of LI. We can write

$$\begin{aligned} c_{33} &= \rho V_{P,0}^2 \quad , \quad c_{55} = \rho V_{S,0}^2, \\ c_{11} &= \rho V_{P,90}^2 \quad , \quad c_{44} = \rho V_{S,90}^2, \end{aligned} \tag{25}$$

where $V_{P,0}$, $V_{P,90}$ and $V_{S,0}$, $V_{S,90}$ are vertical (0) and horizontal (90) P- and S-wave velocities. The difference between c_{11} and c_{33}, as well as that of c_{44} and c_{55}, decreases as LI increases. The azimuth distribution function complies with the uniform distribution in terms of the azimuth angle φ, as illustrated in Eq. 10. By using seismic data, one can estimate LI while neglecting the effect of vertical microfractures. Practically, the inversion can be performed as

$$\mathrm{J(LI)} = ||c_{33}^{\mathrm{obs}} - c_{33}(\mathrm{LI})||_2^2 + ||c_{44}^{\mathrm{obs}} - c_{44}(\mathrm{LI})||_2^2, \tag{26}$$

where J is the objective function, and $\{\cdot\}^{\mathrm{obs}}$ denotes the parameters of observed data. To further clarify the effect of LI, we define

$$\begin{aligned} \zeta_{b,0} &= \frac{c_{55}}{c_{33}} = \frac{\rho V_{S,0}^2}{\rho V_{P,0}^2}, \\ \zeta_{b,90} &= \frac{c_{44}}{c_{11}} = \frac{\rho V_{S,90}^2}{\rho V_{P,90}^2}. \end{aligned} \tag{27}$$

Figure 4 shows that LI has a considerable effect on stiffness, which has a nonlinear effect on the VTI characteristic intensity of the shale. The model for fractured shale has two parts, as stated in Eq. (12), the VTI background and the microfracture

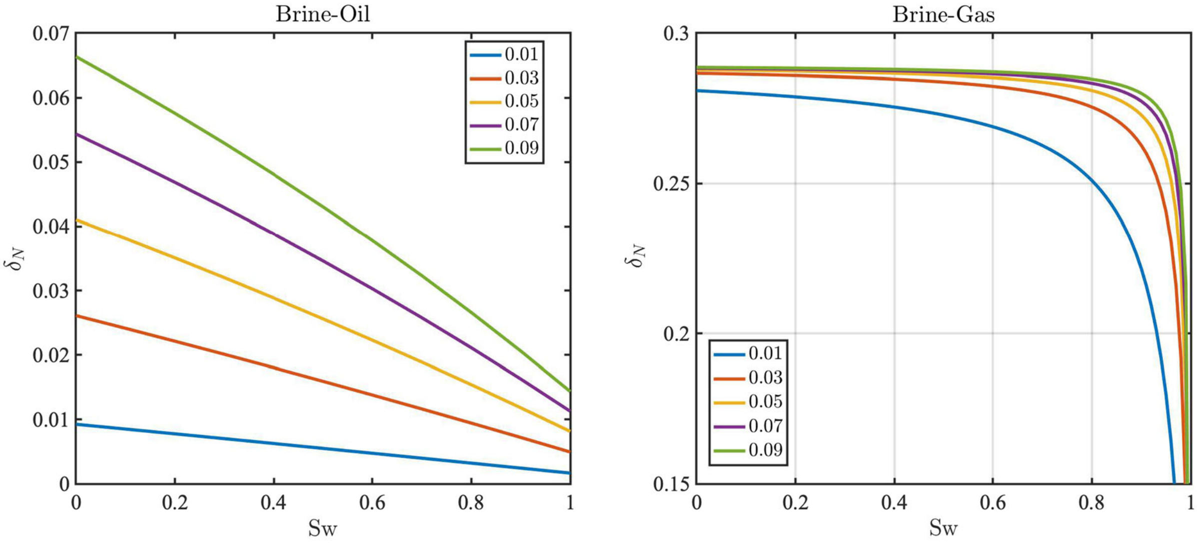

(a) **(b)**

Figure 7
Fracture weakness δ_N as a function of water saturation for various aspect ratio of the fractures χ, corresponding to (**a**) gas–water and (**b**) oil–water

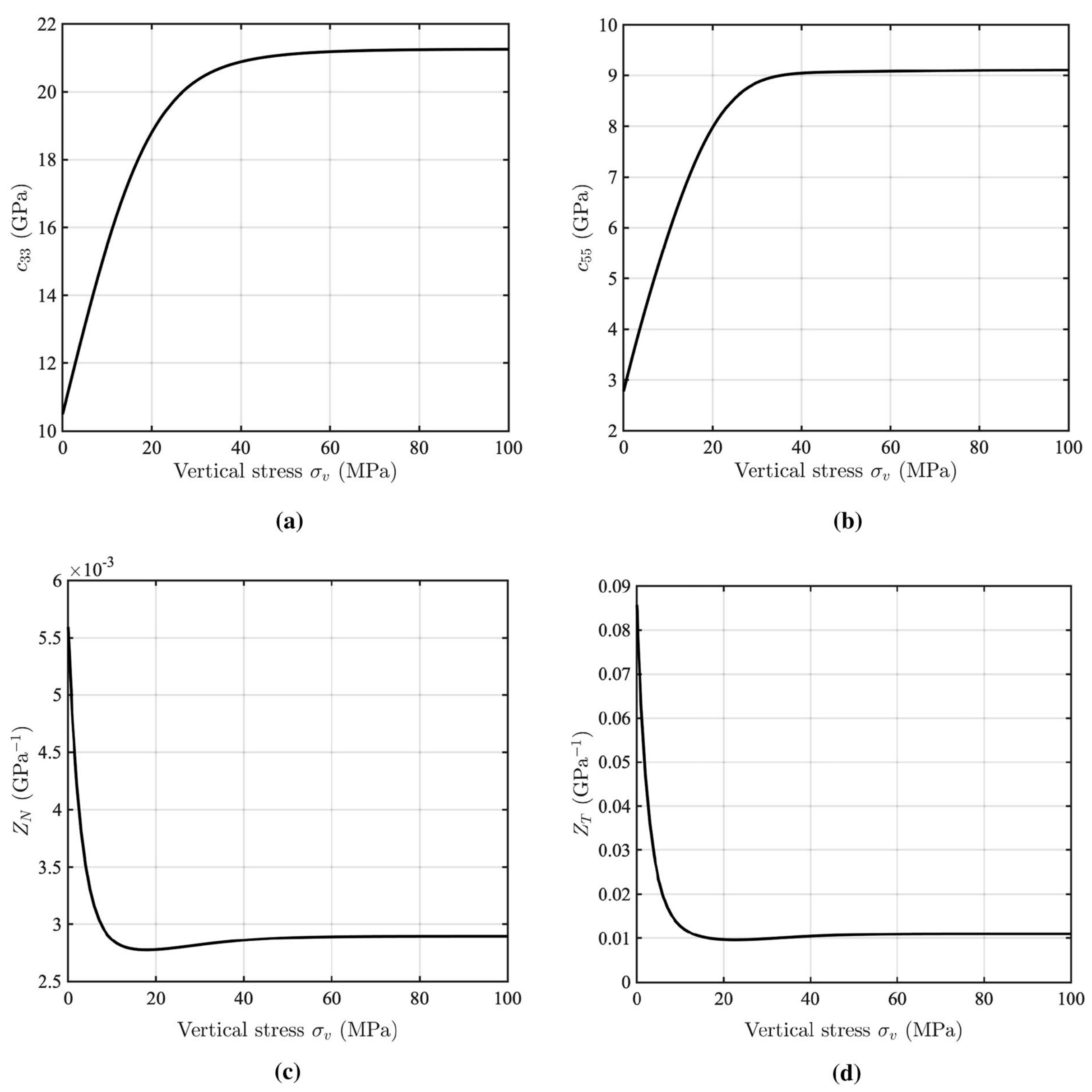

(a) **(b)**

(c) **(d)**

Figure 8

c_{11}, c_{55} and fracture weaknesses Z_N, Z_T as a function of the vertical stress σ_v

perturbation. Both LI and microfracture weakness should be considered in amplitude variations with angle and azimuth (AVAZ). In practice, as given in Eqs. (14) and (15), well-estimated background properties can improve the estimation of accurate microfracture parameters.

3.2. *Effect of Fractures*

We analyze the effects of LI and microfracture properties such as e, χ, and the fluid bulk modulus, on the stiffness and fracture weakness. Table 2 shows the saturating fluid properties. LI affects δ_N and δ_H

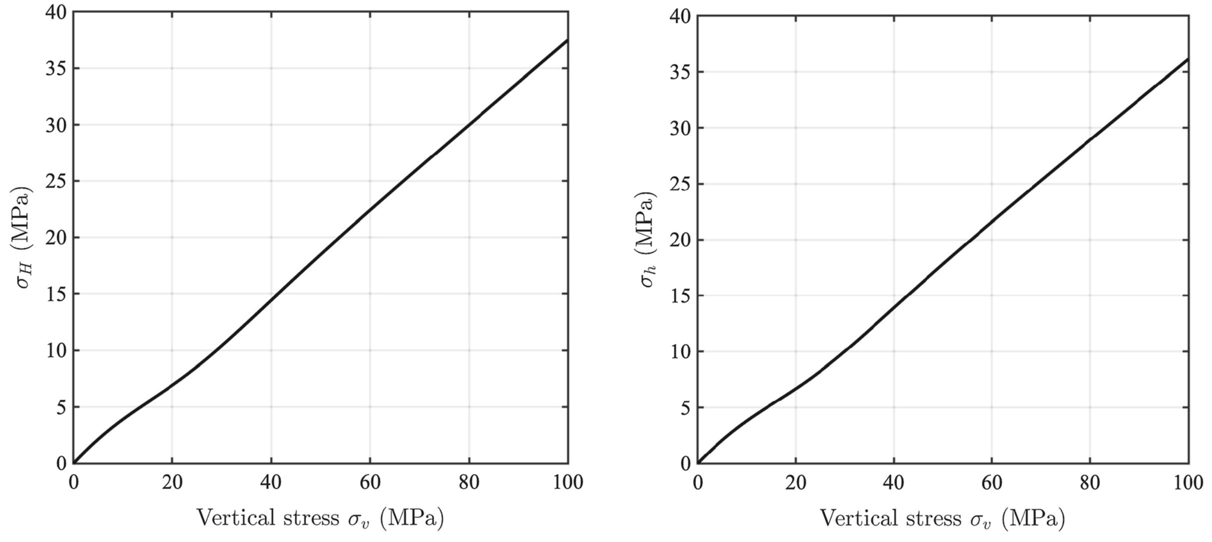

(a) **(b)**

Figure 9
Maximum and minimum horizontal stresses as a function of the vertical stress σ_v

but not δ_V, as shown in Fig. 5. The microfractures are saturated with brine (a, b, c), oil (d, e, f), and gas (g, h, i). The fluid bulk modulus highly affects δN but not δ_V and δ_H; δ_V is only affected by the microfracture density e but not by the other properties. In practice, this suggests to estimate e from δ_V, and Eqs. (16) and (26) can be used to obtain LI; δ_N can be used to estimate the fracture fluid properties.

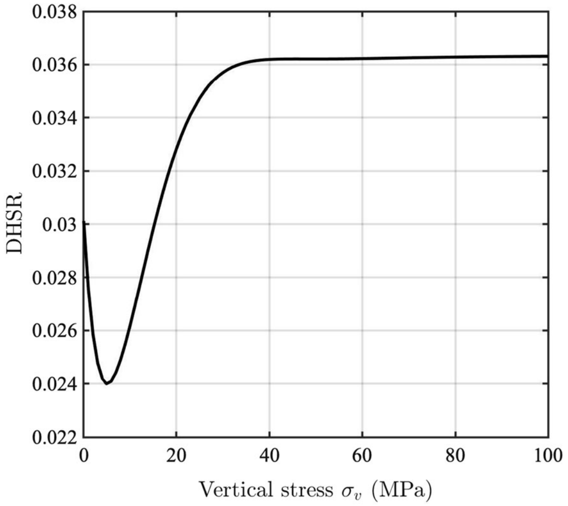

Figure 10
DHSR profile as a function of the vertical stress

Figure 6 shows the stiffness perturbations between the fractured and background shale models (a) Δc_{11}, (b) Δc_{22}, (c) Δc_{33}, (d)Δc_{44}, (e)Δc_{55}, and (f) Δc_{66} as a function of LI and e. The fluid modulus is obtained from the Wood equation

$$Z_{fluid} = S_w Z_w + S_o Z_o + S_g Z_g \tag{28}$$

(Domenico, 1976), where $Z = 1/K$ denotes the compressibility. $\{\cdot\}_{fluid}$, $\{\cdot\}_w$, $\{\cdot\}_o$, and $\{\cdot\}_g$ are the properties of fluid, water, oil, and gas, respectively. The fluid has 90% brine and 10% oil. Thus, one can estimate LI from $V_{P,0} = \sqrt{c_{33}/\rho}$ and $V_{S,90} = \sqrt{c_{44}/\rho}$ by solving the following objective function:

$$\mathrm{J(LI)} = ||V_{P,0}^{\mathrm{obs}} - V_{P,0}^{\mathrm{predict}}(\mathrm{LI})||_2^2 + \alpha||V_{S,90}^{\mathrm{obs}} - V_{S,90}^{\mathrm{predict}}(\mathrm{LI})||_2^2. \tag{29}$$

As is shown in Figure 6, the stiffness perturbations gradually converge to a limitation as LI increases. It means that there is little chance to obtain a reliable large LI parameter.

Figure 7 shows δ_N as a function of the water saturation for various values of the aspect ratio χ. The fluid bulk modulus has an effect in the gas–water case, which can be used to identify the fluid,

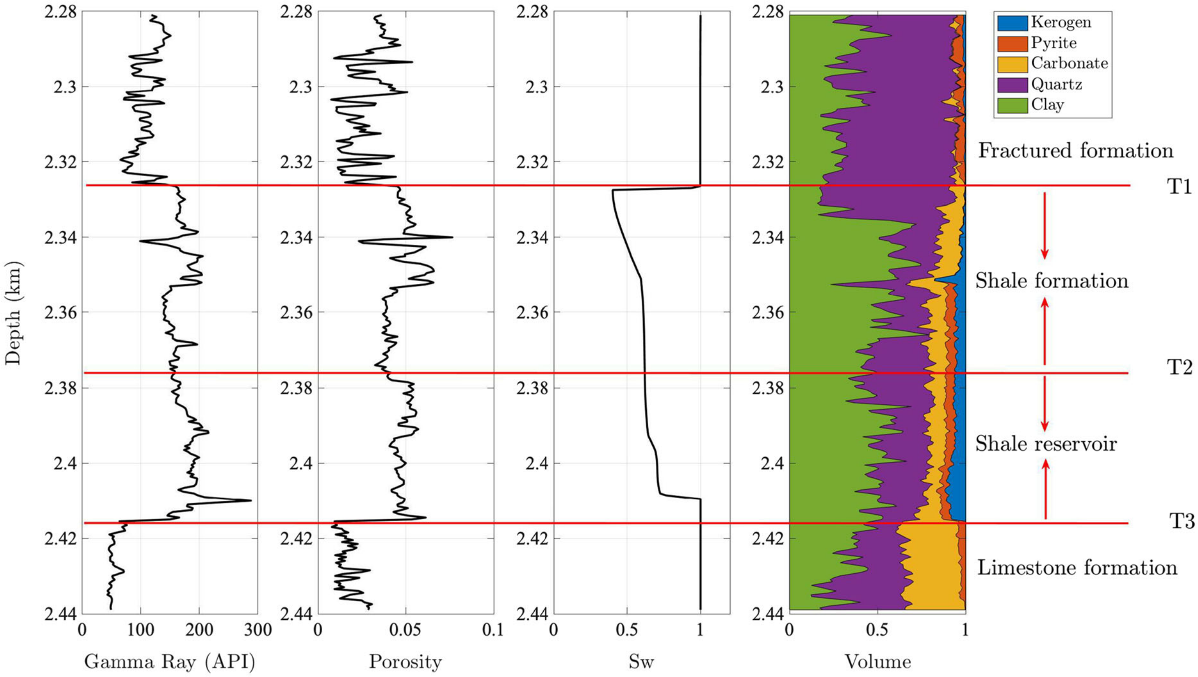

Figure 11
Well-log profiles and interpretation results, including gamma-ray, porosity, water saturation, and volume of minerals

particularly in fractured gas reservoirs. Furthermore, the ratios δ_N/δ_V and δ_N/δ_H can both be used as fluid indicators. Increasing the fracture density increases the fracture weakness and the anisotropy.

In practice, we can estimate accurate LI values from well-log data and mineral elastic parameters using the proposed method. Then, after removing the effect of the background medium, we can implement AVAZ inversion to obtain the fracture weaknesses.

3.3. Effect of Pressure

We use the DZ model to obtain a pressure-dependent stiffness matrix for each mineral as well as the fracture weaknesses. The fractured model is then rebuilt using the method shown in Fig. 1 at various pressures. Here, we refer to Daley et al. (2006) and set $Z_{V\infty} = Z_{V0}/5, Z_{H\infty} = Z_{H0}/5$, $Z_{N\infty} = Z_{N0}/2$, $S_\infty = S_0/2$, and the decay rates $\tau_N = 2$, $\tau_V = 2$, $\tau_H = 2$, and $\tau_S = 10$. Figure 8 shows c_{11}, c_{55} and fracture weakness Z_N, Z_V, Z_H, which gradually increase or decrease with increasing pressure and maintain a constant value beyond a given threshold, approximately 40 MPa. The DZ model provides a reliable theoretical approach to perform the inversion of the fracture properties.

Besides, the estimation of the in situ stress state is important for a successful drilling plan and hydraulic fracturing for optimum economic production. The maximum and minimum horizontal stresses, σ_H and σ_h, of an orthorhombic medium can be derived from the following equation (Gray et al., 2012):

$$\begin{aligned}\sigma_h &= \sigma_v \frac{v(1+v)}{1+EZ_N - v^2}\\ \sigma_H &= \sigma_v \frac{v(1+EZ_N+v)}{1+EZ_N - v^2},\end{aligned} \tag{30}$$

where σ_v is the vertical stress, E and v are Young's modulus and Poisson's ratio of the background mineral, respectively.

Figure 9 shows the calculated maximum and minimum horizontal stresses as a function of the vertical stress. An important indicator in shale fracturing is the differential horizontal stress ratio (DHSR) (Gray et al., 2012):

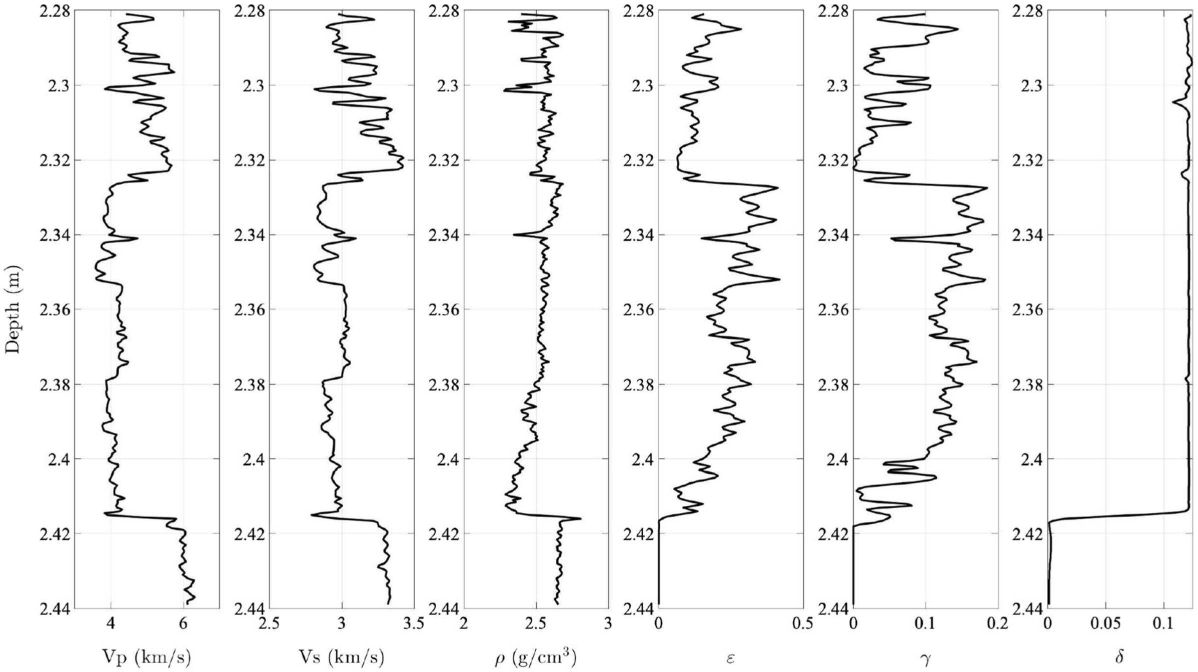

Figure 12
Well-log profiles, including the P- and S-wave velocities, density, and Thomsen parameters

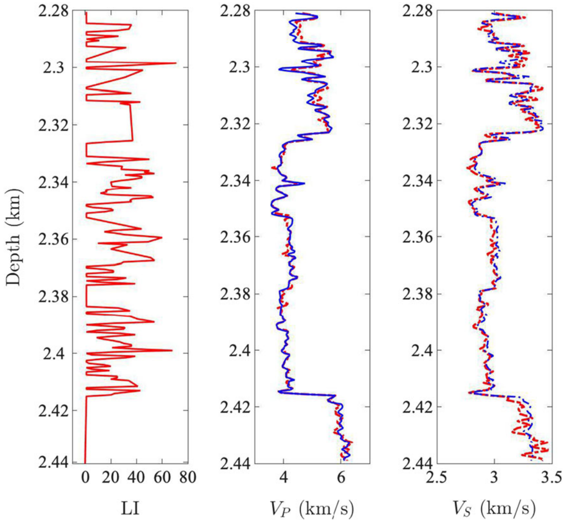

Figure 13
LI and simulated velocity profiles. The solid blue line and red dotted line denote the real well-log profiles and simulations, respectively

$$\mathrm{DHSR} = \frac{\sigma_H - \sigma_h}{\sigma_H}. \tag{31}$$

Generally, a high DHSR value indicates that a high number of microfractures parallel to the maximum horizontal principal stress develop in the formation. Microfractures that are not parallel to the horizontal stress direction can be characterized by this parameter. The DHSR as a function of the vertical stress is shown in Fig. 10. As the vertical principal stress increases, the DHSR value eventually converges to a limited value. Figure 10 shows that when it is greater than 40 MPa, it converges to the limit, but this threshold (40 MPa) depends much on the relationship between Z_∞ and Z_0. In practice, such relationship changes with depth, and the threshold therefore increases with increasing depth.

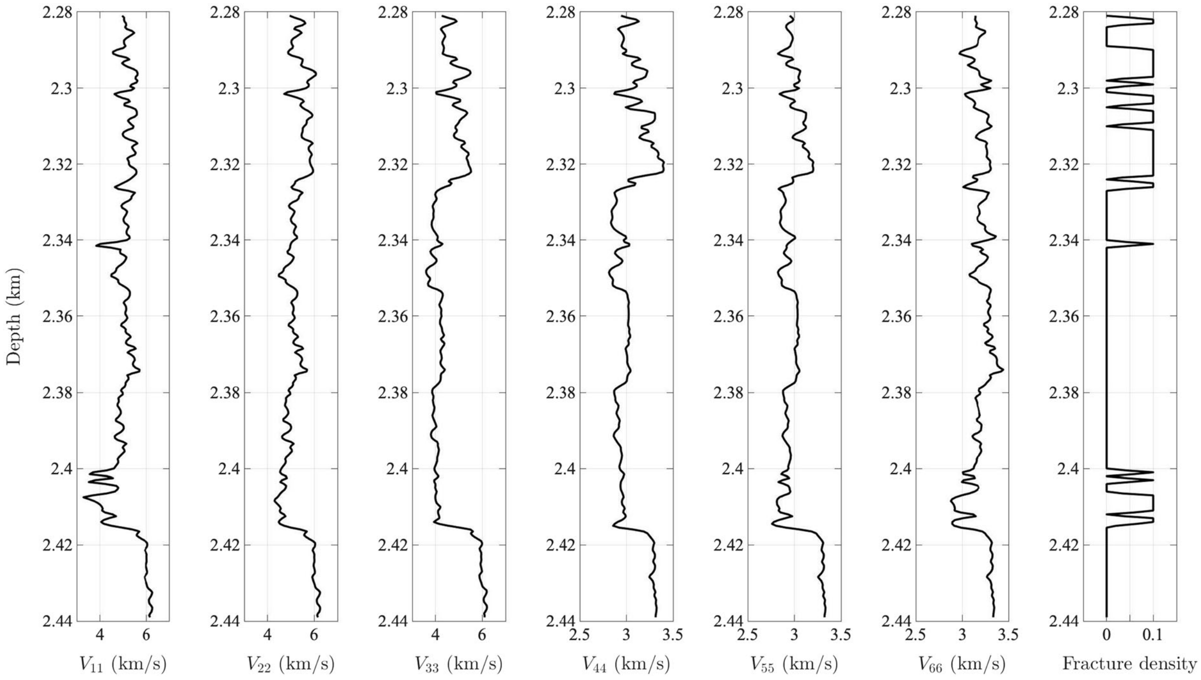

Figure 14
Elastic velocities V_{IJ} after introducing the vertical fractures and fracture density

4. *Well-data Verification*

We validate the model with well-log profiles collected from southwestern China. The well logs and interpretation, which include gamma-ray, porosity, water saturation, and volume of minerals, are shown in Fig. 11. The reservoir, located at the bottom of the shale formation underlain by a limestone stratum, is characterized by a high gamma-ray value and porosity. The rightmost panel shows the mineral fractions, where we can see that clay and quartz are dominant, as well as kerogen, while the limestone layers have a high amount of carbonate minerals. Here, we mainly concentrate on the shale formation, i.e., the T1 to T3 range. Well-log profiles, including P- and S-wave velocities, density, and Thomsen parameters, are shown in Fig. 12.

The inversion approach estimates LI by using the P- and S-wave velocities as a reference. The simulated velocity profiles and the resulting LI profiles are shown in Fig. 13. The log profiles are obtained from the formation without fractures. Thus, we add the fracture effects to the logs to test the validity of the model. The fracture density is displayed in Fig. 14. We also represent the velocities associated with the various stiffness values, where $V_{IJ} = \sqrt{c_{IJ}/\rho}$.

In Fig. 15, we explain how to simulate the well-log profiles step by step using the fractured shale model. Figure 15a shows the simulation under normal pressure, LI, and fractures. When pressure is introduced, there are still differences with the observed values (see Fig. 15b). When the LI effects are considered (Fig. 15c), we can see that the P-wave velocity is simulated properly, but there are differences in the S-wave. Finally, introducing the fracture effects, both the modeled P-wave and S-wave velocities have a good agreement with the observed values, as shown in Fig. 15d.

5. *Conclusions*

We have presented a comprehensive methodology for modeling the elastic properties of a pressure-dependent fractured and laminated shale with different

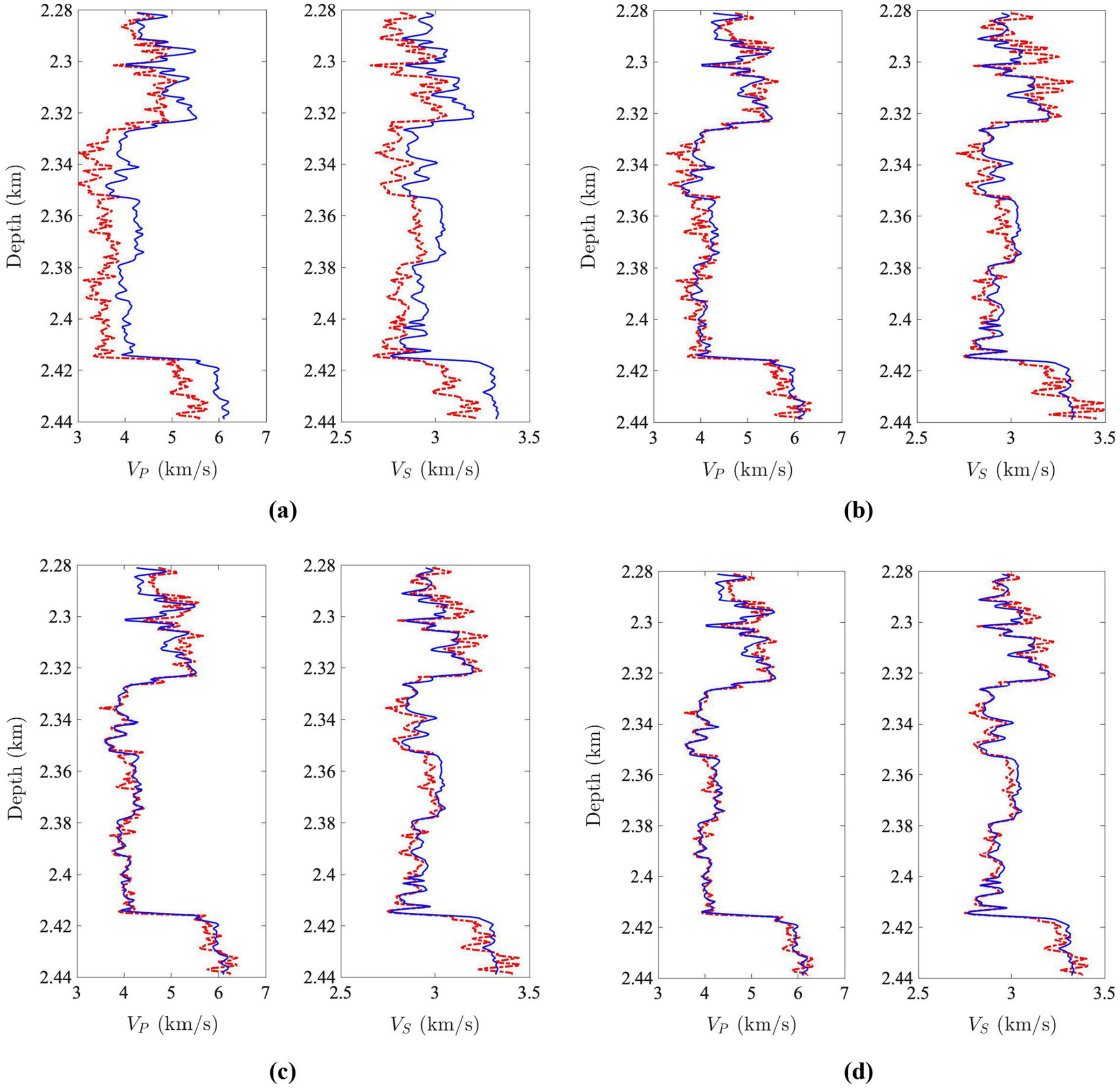

Figure 15
Simulated well-log profiles (**a**) without pressure, LI, and fractures, (**b**) with pressure but without LI and fractures, (**c**) with pressure and LI but without fractures, and (**d**) with all these properties

degrees of maturation. The effective medium is represented by the orthotropic class, which is a result of combining the lamination (transverse isotropy) and vertical fractures. Many factors regarding the intrinsic anisotropy of shale are taken into account, wherein clay lamination and fractures show a greater impact on the shale anisotropy. The preferred orientation of clay, which is an important factor affecting the VTI properties of background medium, is parameterized by the standard deviation of the ODF. The Hudson and Schoenberg models are combined and included in the workflow to simulate the microfracture-induced anisotropy. Unlike the LI parameter, the numerical analysis shows that the microfracture only affects some elasticity. Thus, such microfracture-independent constants can be used as a baseline inversion of the LI, and the fracture parameters is then retrieved based on the obtained LI. Well-log data examples demonstrate the proposed rock physics workflow can effectively simulate the intrinsic anisotropy of fractured shale.

Acknowledgements

This work was supported in part by the National Natural Science Foundation of China under Grant 42004111, in part by Jiangsu Innovation and Entrepreneurship Plan, and in part by Jiangsu Province Science Fund for Distinguished Young Scholars (grant no. BK20200021).

REFERENCES

Ahmadov, R. (2011). Microtextural, elastic and transport properties of sourcerocks: Ph.D. thesis, Stanford University.

Backus, G. E. (1962). Long-wave elastic anisotropy produced by horizontal layering. *Journal of Geophysical Research, 67*, 4427–4440.

Bakulin, A., Grechka, V., & Tsvankin, I. (2000). Estimation of fracture parameters from reflection seismic data-part I: HTI model due to a single fracture set. *Geophysics, 65*, 1788–1802.

Bakulin, A., Grechka, V., & Tsvankin, I. (2000). Estimation of fracture parameters from reflection seismic data-part II: Fractured models with orthorhombic symmetry. *Geophysics, 65*, 1803–1817.

Bayuk, I. O., Ammerman, M., & Chesnokov, E. M. (2007). Elastic moduli of anisotropic clay. *Geophysics, 72*(5), D107–D117.

Bandyopadhyay, K. (2009). Seismic anisotropy: Geological causes and its implications to reservoir geophysics, PhD Thesis, Stanford University.

Bandyopadhyay, K., Sain, R., Liu, E., Harris, C., Martinez, A., Payne, M., & Zhu Y. (2012). Rock property inversion in organic-rich shale: Uncertainties, ambiguities, and pitfalls. The 82nd Annual International Meeting, Society of Exploration Geophysicists. Expanded Abstracts, 1-5.

Berryman, J. G. (1980). Long-wavelength propagation in composite elastic media II. *Ellipsoidal inclusions: The Journal of the Acoustical Society of America, 68*(6), 1820–1831.

Blanton, T., Olson, J. E. (1999). Stress magnitudes from logs: Effects of tectonic strains and temperature. *SPE Reservoir Evaluation & Engineering, 2*(1), 62–68.

Bond, W. L. (1943). The mathematics of the physical properties of crystals. *The Bell System Technical Journal, 22,* 1–72.

Carcione, J. M. (2000). A model for seismic velocity and attenuation in petroleum source rocks. *Geophysics, 65*, 1080–1092.

Carcione, J. M., Helle, H. B., & Avseth, P. (2011). Source-rock seismic-velocity models: Gassmann versus Backus. *Geophysics, 76,* N37–N45.

Carcione, J., Picotti, S., & Santos, J. E. (2012). Numerical experiments of fracture-induced velocity and attenuation anisotropy. *Geophysical Journal International, 191*, 1179–1191.

Carcione, J. M., Santos, J. E., Picotti, S., & S. (2012). Fracture-induced anisotropic attenuation. *Rock Engineering, 45,* 929–942.

Carcione, J. M., & Picotti, S. (2012). Reflection and transmission coefficients of a fracture in transversely isotropic media. *Studia Geophysica et Geodaetica, 56*, 307–322.

Carcione, J. M., Gurevich, B., Santos, J. E., & Picotti, S. (2013). Angular and frequency-dependent wave velocity and attenuation in fractured porous media. *Pure and Applied Geophysics, 170*, 1673–1683.

Carcione, J. M., & Avseth, P. (2015). Rock-physics templates for clay-rich source rocks. *Geophysics, 80,* D481–D500.

Carcione, J. M., Farina, B., Poletto, F., Qadrouh, A. N., & Cheng, W. (2020). Seismic attenuation in partially molten rocks. *Physics of the Earth and Planetary Interiors, 309*, 106568.

Carcione, J. M., Gei, D., Picotti, S., Qadrouh, A. N., Alajmi, M., & Ba, J. (2021). Rock acoustics of diagenesis and cementation, Rock acoustics of diagenesis and cementation. arXiv preprint arXiv:2111.07743.

Carmichael, R. S. (1988). Practical handbook of physical properties of rocks and minerals: CRC Press.

Crampin, S. (1984). Effective anisotropic elastic constants for wave propagation through cracked solids. *Geophysical Journal International, 76*, 135–145.

Daley, T. M., Schoenberg, M. A., Rutqvist, J., & Nihei, K. T. (2006). Fractured reservoirs: An analysis of coupled elastodynamic and permeability changes from pore-pressure variation. *Geophysics, 71*(5), O33–O41.

David, E., & Zimmerman, R. W. (2012). Pore structure model for elastic wave velocities in fluid-saturated sandstones. *Journal of Geophysical Research: Solid Earth, 117,* B07210.

Derbyshire, F. (1991). Vitrinite structure: alterations with rank and processing. *Fuel, 70*, 276–284.

Eastwood, R. L., & Castagna, J. P. (1987). Interpretation of Vp/Vs ratios from sonic logs: Shear wave exploration. *Geophysical Development Service, 1*, 139–153.

Gray, David, Anderson, Paul, Logel, John, et al. (2012). Estimation of stress and geomechanical properties using 3D seismic data. *First Break, 30*(3), 59–68.

Guo, Z., Li, X., Liu, C., Feng, X., & Shen, Y. (2013). A shale rock physics model for analysis of brittleness index, mineralogy and porosity in the barnett shale. *Journal of Geophysics and Engineering, 10,* 025006.

Guo, Z., Li, X., & Liu, C. (2014). Anisotropy parameters estimate and rock physics analysis for the barnett shale. *Journal of Geophysics and Engineering, 11*, 065006.

Hill, R. (1952). The elastic behaviour of a crystalline aggregate. Proceedings of the Physical Society. Section A, **65**, 349.

Hornby, B. E., Schwartz, L. M., & Hudson, J. A. (1994). Anisotropic effective-medium modeling of the elastic properties of shales. *Geophysics, 59*, 1570–1583.

Hsu, C. J., & Schoenberg, M. (1993). Elastic waves through a simulated fractured medium. *Geophysics, 58*, 964–977.

Hudson, J. A. (1981). Wave speeds and attenuation of elastic waves in material containing cracks. *Geophysical Journal International, 64*, 133–150.

Hui, Z., Yang, X., Hu, Q. Z., & Cheng, C. B. (2011). Strength test and mechanism of softening of chlorite schist. *Soil Engineering and Foundation, 25,* 45.

Humbert, P., et al. (1972). Proprietés élastiques de carbonates rhomboédriques monocristallins: calcite, magnésite, dolomie: Computes Rendus de l'Academie des Sciences, **275**, no. B, 391-394.

Luo, X., & Vasseur, G. (1996). Geopressuring mechanism of organic mattercracking: Numerical modeling. *AAPG Bulletin, 80*, 856–874.

Johnston, J. E., & Christensen, N. I. (1995). Seismic anisotropy of shales. *Journal of Geophysical Research, 100*(B4), 5991–6003.

Jones, L. E., & Wang, H. F. (1981). Ultrasonic velocities in Cretaceous shales from the Williston basin. *Geophysics, 46*(3), 288–297.

Li, Yang, Wu, Xiaoyang, & Chapman, Mark. (2015). Impacts of kerogen content and fracture properties on the anisotropic seismic reflectivity of shales with orthorhombic symmetry. Interpretation, **3**, (3), ST1-ST7.

Mavko, G., Mukerji, T., & Dvorkin, J. (2020). The rock physics handbook. Cambridge University Press.

Mukerji, T., Berryman, J., Mavko, G., et al. (1995). Differential effective medium modeling of rock elastic moduli with critical porosity constraints. *Geophysical Research Letters, 22*(7), 555–558.

Oh, J. W., & Alkhalifah, T. (2016). The scattering potential of partial derivative wave-fields in 3-D elastic orthorhombic media: An inversion prospective. *Geophysical Journal International, 206,* 1740–1760.

Pinna, G., Carcione, J. M., & Poletto, F. (2011). Kerogen to oil conversion in source rocks. Pore-pressure build-up and effects on seismic velocities. *Journal of Applied Geophysics, 74,* 229–235.

Qian, K., Zhang, F., Chen, S., Li, X., & Zhang, H. (2016). A rock physics model for analysis of anisotropic parameters in a shale reservoir in southwest china. *Journal of Geophysics and Engineering, 13*, 19–34.

Sayers, C. (2005). Seismic anisotropy of shales. *Geophysical Prospecting, 53,* 667–676.

Sayers, C. M., & den Boer, L. D. (2018). The elastic properties of clay in shales. *Journal of Geophysical Research: Solid Earth, 123*(7), 5965–5974.

Schoenberg, M. (1980). Elastic wave behavior across linear slip interfaces. *The Journal of the Acoustical Society of America, 68*, 1516–1521.

Schoenberg, M., & Douma, J. (1988). Elastic wave propagation in media with parallel fractures and aligned cracks. *Geophysical Prospecting, 36*(6), 571–590.

Schoenberg, M., & Sayers, C. M. (1995). Seismic anisotropy of fractured rock. *Geophysics, 60*(1), 204–211.

Simmons, G., & Birch, F. (1963). Elastic constants of pyrite. *Journal of Applied Physics, 34*, 2736–2738.

Simmons, G. (1965). Single crystal elastic constants and calculated aggregate properties. Technical report, Southern Methodist Univ Dallas Tex.

Tabaeh, H. M., & Mohammad, A. (2016). Estimation of in-situ horizontal stresses using the linear poroelastic model and minifrac test results in tectonically active area. *Russian Journal of Earth Sciences, 16*(4), 1–9.

Tissot, B., Durand, B., Espitalie, J., & Combaz, A. (1974). Influence of nature and diagenesis of organic matter in formation of petroleum. *AAPG Bulletin, 58,* 499–506.

Vanorio, T., Prasad, M., & Nur, A. (2003). Elastic properties of dry clay mineral aggregates, suspensions and sandstones. *Geophysical Journal International, 155,* 319–326.

Vernik, L., & Nur, A. (1992). Ultrasonic velocity and anisotropy of hydrocarbon source rocks. *Geophysics, 57*(5), 727–735.

Vernik, L., & Landis, C. (1996). Elastic anisotropy of source rocks: Implicationsfor hydrocarbon generation and primary migration. *AAPG Bulletin, 80*, 531–544.

Vernik, L., & Liu, X. (1997). *Velocity anisotropy in shales: A petrophysicalstudy: Geophysics, 62*, 521–532.

Wang, Z., Wang, H., & Cates, M. E. (2001). *Effective elastic properties of solid clays: Geophysics, 66*, 428–440.

Wang, Z. (2002). Seismic anisotropy in sedimentary rocks, part 2: Laboratory data: Geophysics,**67**, 1423-1440.

Willis, J. R. (1977). Bounds and self-consistent estimates for the overall properties of anisotropic composites. *Journal of the Mechanics and Physics of Solids, 25*(3), 185–202.

Xu, S., & White, R. E. (1995). *A new velocity model for clay-sand mixtures: Geophysical prospecting, 43*(1), 91–118.

Xu, S., Saltzer, R. L., & Keys, R. G. (2010). Integrated anisotropic rock physics model. (US Patent 7,676,349).

Yan, F., & Han, D. (2013). *Measurement of elastic properties of kerogen: 83rd Annual International Meeting* (pp. 2778–2782). Expanded Abstracts: SEG.

Zhang, F., Li, X., Qian, K. (2017). Estimation of anisotropy parameters for shale based on an improved rock physics model, part 1: theory: Journal of Geophysics and Engineering, **14**, 143-158.

Zhang, F. (2017). Estimation of anisotropy parameters for shales based on an improved rock physics model, part 2: case study: Journal of Geophysics and Engineering, **14**, 238-254.

Zhang, L., Ba, J., Fu, L., Carcione, J. M., & Cao, C. (2019). Estimation of pore microstructure by using the static and dynamic moduli. *International Journal of Rock Mechanics and Mining Sciences, 113*, 24–30.

Zhao, L., Qin, X., Han, D., Geng, J., Yang, Z., & Cao, H. (2016). Rock-physics modeling for the elastic properties of organic shale at different maturity stages. *Geophysics, 81*, D527–D541.

Zimmerman, R. W. (1991). Compressibility of sandstones: Elsevier.

Zoback, M. D. (2010). Reservoir geomechanics: Cambridge university press.

(Received July 5, 2022, revised August 23, 2022, accepted September 16, 2022, Published online October 25, 2022)